Electronic Supplementary Information

Highly selective electroreduction of CO_2 to CO with ZnO QDs/N-doped porous carbon catalysts

Zijian Fang,[a,1] Yanling Zhai,[a,1] Weiwei Guo,[a,] Zhaoyang Sun,[a] Lei Jiao,[a] Zhijun Zhu,[a,*] Xiaoquan Lu,[a,*] Jianguo Tang[a,*]*

[a] *Institute of Hybrid Materials, College of Materials Science and Engineering, Institute of Molecular Metrology, College of Chemistry and Chemical Engineering, Qingdao University, Qingdao, 266071, P. R. China.*

[1] *These authors contributed equally to this work.*
**E-mail: guoweiwei21@qdu.edu.cn (W.G.), zhuzhijun@qdu.edu.cn (Z.Z.), tang@qdu.edu.cn (J. Tang), luxq@nwnu.edu.cn (X.L.)*

Experimental Section

Materials

Dicyandiamide, sulfuric acid, glucose ($C_6H_{12}O_6$), acetone and $KHCO_3$ (AR, 99.5%) were purchased from Sinopharm Chemical Reagent Co., Ltd (China). Hydrofluoric acid (HF), zinc acetate dihydrate ($Zn(CH_3COO)_2{\cdot}2H_2O$) and zinc chloride ($ZnCl_2$) were purchased from Shanghai Macklin Biochemical Technology Co., Ltd (China). Glucosamine hydrochloride and KOH (AR, 95%) were obtained from Aladdin Reagent Co., Ltd (China). Colloidal silica (40 wt.% suspension in H_2O) was purchased from Sigma-Aldrich (US). Nafion N-117 membrane (0.180 mm thick), Nafion D-520 dispersion (5% w/w in water and 1-propanol) and Carbon Paper (CP) were obtained from Alfa Aesar Co., Ltd. 1-butyl-3-methylimidazole hexafluorophosphate ([Bmim]PF_6, > 99%) was obtained from the Green Chemistry and Catalysis Center (China). CO_2 (> 99.999%) was provided by Qingdao Telilai Trading Co., Ltd (China).

Catalysts preparation

Synthesis of porous N-doped carbon: 5 mL of colloidal silica, 334 mg of $ZnCl_2$, 2.5 g glucosamine hydrochloride, 2.5 g dicyandiamide, and 25 mL of deionized water were mixed and stirred for 2 h. After the lyophilization treatment, the obtained ivory powder was heated at 900 ℃ for 2 h at a heating rate of 5 ℃/min in a tube furnace in the presence of N_2. Then the black powder was washed with HF (10%) to obtain porous N-doped carbon (P-NC). N-doped carbon (NC) was prepared with a similar protocol without the addition of colloidal silica. Porous N-doped carbon with different porous structures (P_x-NC) was obtained with a similar procedure except by adding 0 mg $ZnCl_2$, 2.5 mL colloidal silica and 1 mL colloidal silica for P_1-NC, P_2-NC and P_3-NC, respectively. Porous N_1-doped carbon with different N content (P-N_1C and P-C) was obtained with a similar procedure except by adding 5.0 g glucosamine hydrochloride and 5.0 g $C_6H_{12}O_6$ for P-N_1C and P-C, respectively.

Synthesis of porous carbon-supported ZnO quantum dots: 1.5 mmol of $Zn(CH_3COO)_2{\cdot}2H_2O$ and 200 mg P-NC were mixed in 35 mL ethanol and sonicated, then the mixture was heated to 80 ℃ and maintained for 2 h. Then, 1.5 mL of 0.5 M KOH in ethanol was added to the above mixture under stirring after the mixture was cooled to 40 ℃. The obtained suspension was centrifuged and washed with deionized water and ethanol several times before being dried in a vacuum oven at 60 ℃ for 12 h. ZnO_{QDs}/NC, ZnO_{QDs}/P_1-NC, ZnO_{QDs}/P_2-NC, and ZnO_{QDs}/P_3-NC were obtained with a similar procedure using NC, P_1-NC, P_2-NC and P_3-NC as a carrier, respectively. ZnO_{QDs}/P-N_1C and ZnO_{QDs}/P-C were obtained with a similar procedure using P-N_1C and P-C as carrier, respectively.

Catalysts characterization

The morphological and structural characteristics of the materials were obtained from JEOL JEM-F200 high-resolution transmission electron microscopy (HR-TEM) equipped with energy-dispersive X-ray spectroscopy (EDX, OXFORD X-Max). The actual compositions of Zn in the ZnO_{QDs}/P-NC catalysts were determined by inductively coupled plasma optical emission spectroscopy (ICP-OES, PE Avio 200). X-ray photoelectron spectroscopy (XPS) analysis was performed on the Thermo Scientific K-Alpha using 200 W monochromatic Al Kα radiation. The 500 μm X-ray spot was used. The base pressure in the analysis chamber was about 3×10^{-10} mbar. Typically, the hydrocarbon C1s line at 284.8 eV from adventitious carbon was used for energy

referencing X-ray diffraction (XRD) analysis of the samples was performed on the X-ray diffractometer (Rigaku Smartlab SE) with Cu-Kα radiation, and the scan speed was 5° min^{-1}. Raman spectra were recorded on a micro-Raman spectrometer (Renishaw in Via). N_2 adsorption/desorption isotherms of the materials were determined using Micromeritics ASAP 2020 to obtain Brunauer-Emmett-Teller (BET) specific surface area and pore size. The adsorption isotherms of CO_2 were determined at 25 ℃ in the pressure range of 0-1 atm on a TriStar II 3020 device.

Electrode preparation

A mixture of 5 mg of catalyst and 5 μL of Nafion D-520 in 1 mL of acetone was sonicated for 10 min. 500 μL of the as-prepared ink was dropped onto a carbon paper (CP, 0.5 × 2 cm^{-2}) to obtain the working electrode.

Electrocatalytic CO_2 reduction

Electrochemical measurements were carried out on a CHI660E workstation via a two-compartment cell separated by a Nafion 117 membrane in 0.5 M 1-butyl-3-methylimidazolium hexafluorophosphate ([Bmim]PF_6)/MeCN electrolyte saturated with N_2 or CO_2. All measurements were conducted at room temperature in a standard three-electrode system. The as-prepared catalysts on CP, Ag/Ag^+ (0.01 mol L^{-1} $AgNO_3$ in 0.1 mol L^{-1} TBAP-MeCN), and platinum gauze were used as working electrodes, the reference electrode, and the counter electrode, respectively.

Product analysis

The gaseous products were analyzed on gas chromatography (GC, PANNA A60) equipped with FID and TCD detectors using helium as the internal standard. Standard gases are used for calibration to quantify the gas components with conversion coefficients. The liquid products were analyzed on a proton nuclear magnetic resonance spectrometer (^{1}H-NMR, Bruker Avance III 400 HD).

The Faraday efficiency of gas products was calculated by the Eq

$$\mathbf{FE} = \frac{\mathbf{n \cdot N_A \cdot e \cdot V \cdot \nu \cdot P / R \cdot T}}{\mathbf{I_{total} \cdot t}} \mathbf{X\ 100\%}$$

(n: transfer electron number; N_A: Avogadro constant; *v*: gas-flow rate; P: standard atmospheric pressure; R: gas constant; T: temperature; I: total current; t: reaction time)

Tafel analysis

The partial current density of CO was measured at different potentials and the equilibrium potential was known by extrapolation. The overpotential was obtained from the difference between the equilibrium potential and the applied potential. Repeated electrolysis experiments were performed at each potential to obtain data on the overpotential and partial current density of CO in the H-type electrolytic cell. Finally, the tafel plots were plotted.

Electrochemical surface areas (ECSAs) study

The electrochemical active surface area of different electrodes was characterized. It could be determined by measuring the capacitive current associated with double-layer charging (Cdl) from the square root of scan-rate dependence of cycle voltammetry curves (CVs). Cyclic voltammetry was performed in 0.5 M [Bmim]PF_6/ MeCN as the electrolyte using a three-electrode system at 25 °C. Cyclic voltammograms were measured at different scan rates of 25, 75, 125, 175, 225, 275, 325, 375, 425, 475, 525 575 and 625mV s^{-1} at -1.61 to -1.71 V vs. Ag/Ag^+ for the catalysts, and the double layer capacitance (Cdl) of the catalysts were obtained. Cdl was estimated by plotting Δj (ja - jc) at -1.66 V vs. Ag/Ag^+ versus the scan rate, where ja and jc were the anode and cathode current densities, respectively. The linear slope was equivalent to twice the Cdl.

Electrochemical impedance spectroscopy (EIS) study

The experimental apparatus was the same as that for LSV measurements. The EIS measurement was carried out in 0.5 M [Bmim]PF_6/MeCN at an open circuit potential (OCP).

Supplementary Figures

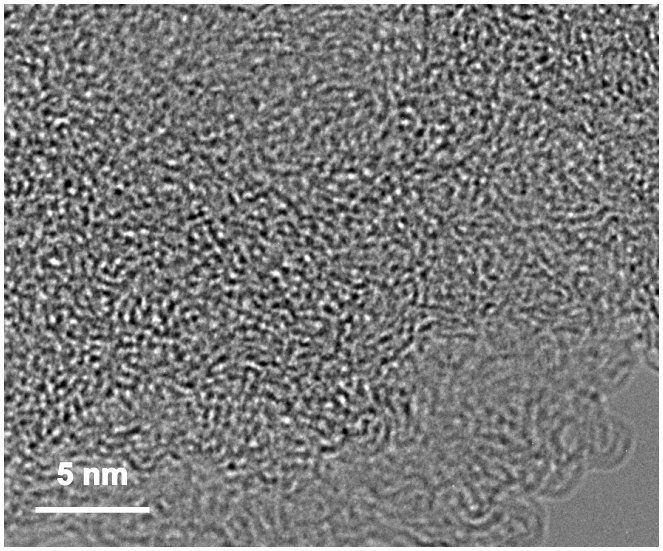

Fig. S1. The HR-TEM image of P-NC.

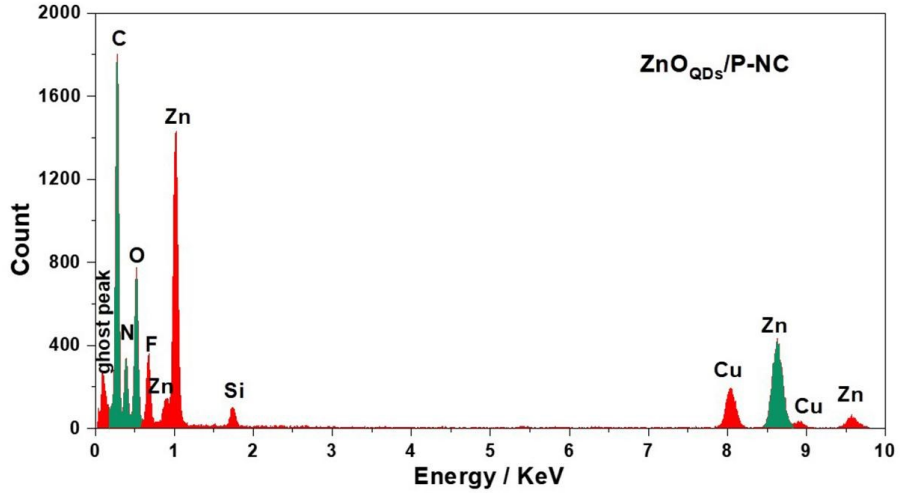

Fig. S2. The distribution diagram of the elements of ZnO_{QDs}/P-NC.

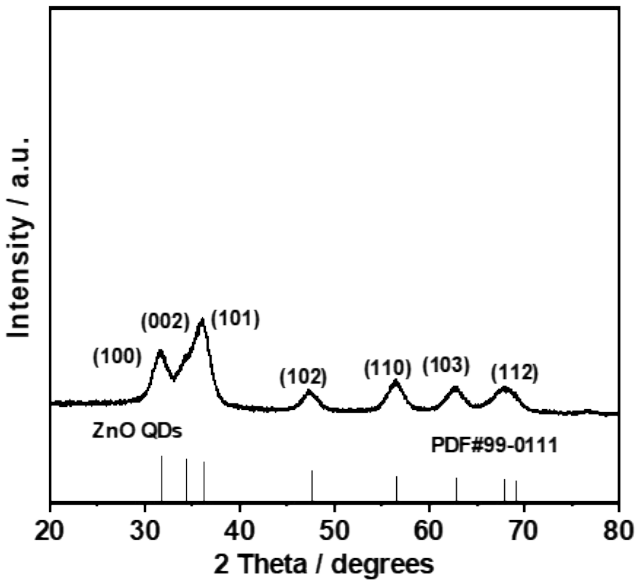

Fig. S3. The XRD pattern of ZnO QDs.

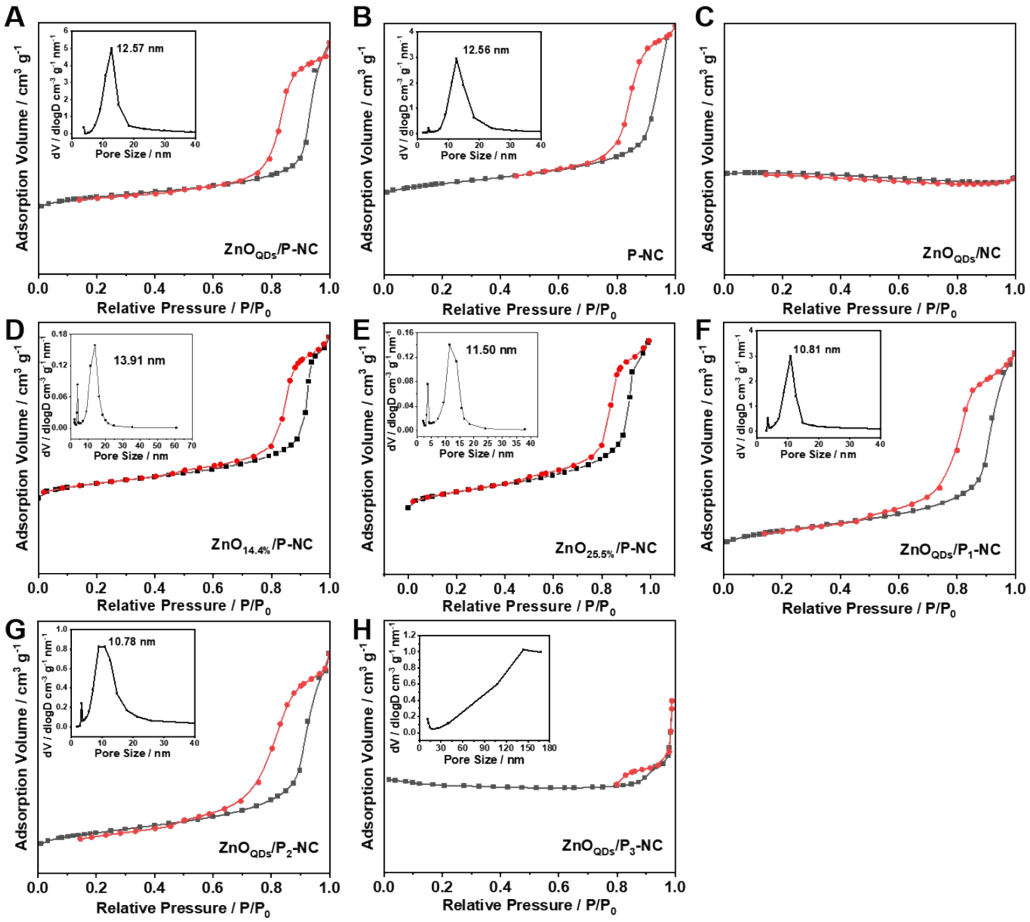

Fig. S4. The N_2-adsorption/desorption isotherms average pore size distribution of (A) ZnO_{QDs}/P-NC, (B) P-NC, (C) ZnO_{QDs}/NC, (D) $ZnO_{14.4\%}$/P-NC, (E) $ZnO_{25.2\%}$/P-NC, (F) ZnO_{QDs}/P_1-NC, (G) ZnO_{QDs}/P_2-NC and (H) ZnO_{QDs}/P_3-NC.

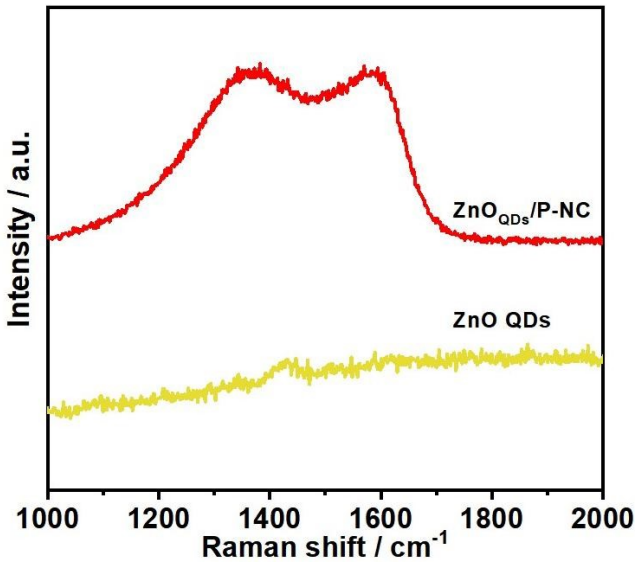

Fig. S5. The Raman spectra of ZnO_{QDs}/P-NC and ZnO QDs.

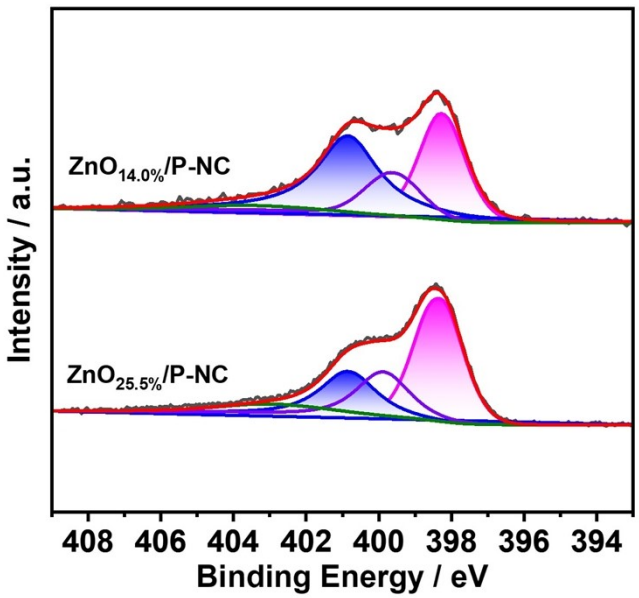

Fig. S6. The XPS spectra of N 1s for $ZnO_{14.0\%}$/P-NC and $ZnO_{25.5\%}$/P-NC.

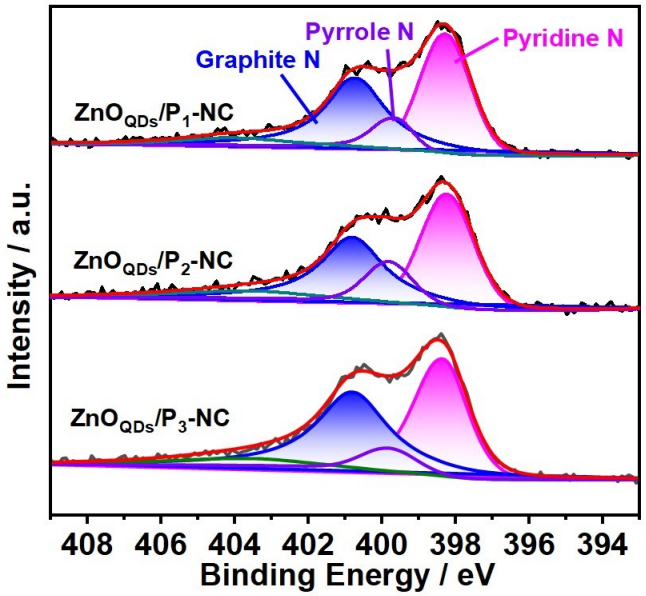

Fig. S7. The XPS spectra of N 1s for ZnO_{QDs}/P_1-NC, ZnO_{QDs}/P_2-NC and ZnO_{QDs}/P_3-NC.

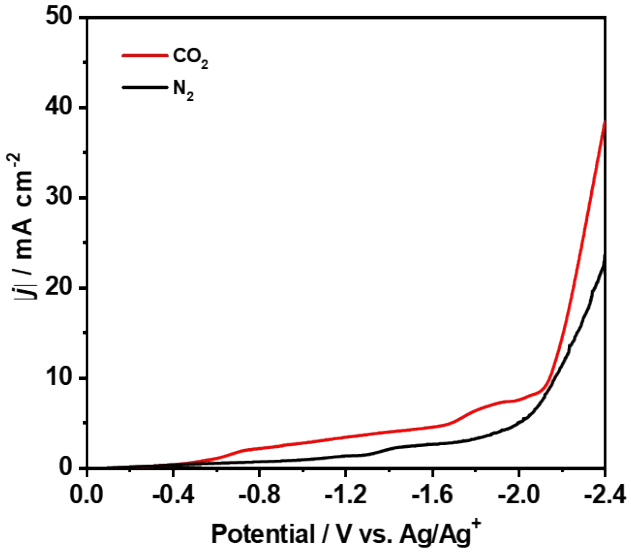

Fig. S8. The LSV curves of ZnO_{QDs}/P-NC in CO_2-saturated and N_2-saturated 0.5 M [Bmim]PF_6/MeCN electrolytes, respectively.

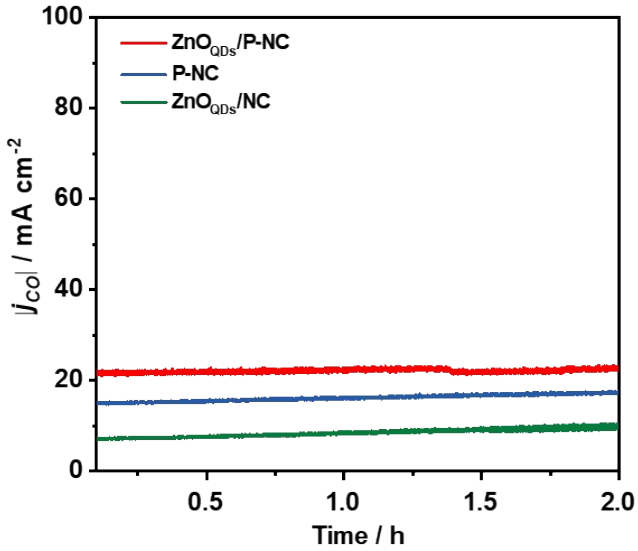

Fig. S9. The stability of different catalysts at -2.2 V vs. Ag/Ag^{+} during 2 h electrolysis.

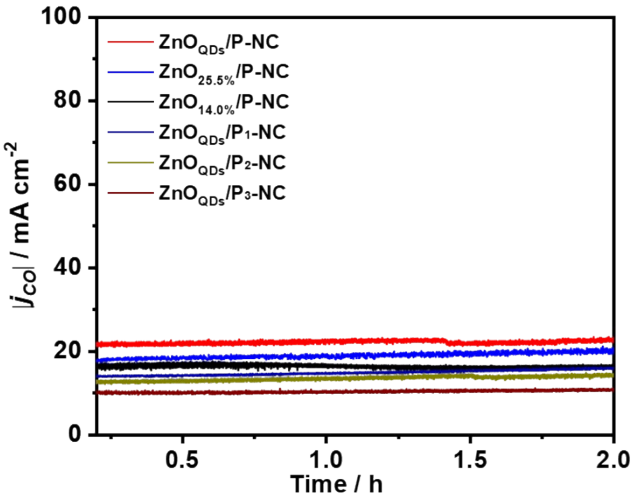

Fig. S10. The stability of different catalysts at -2.2 V vs. Ag/Ag^{+} during 2 h electrolysis.

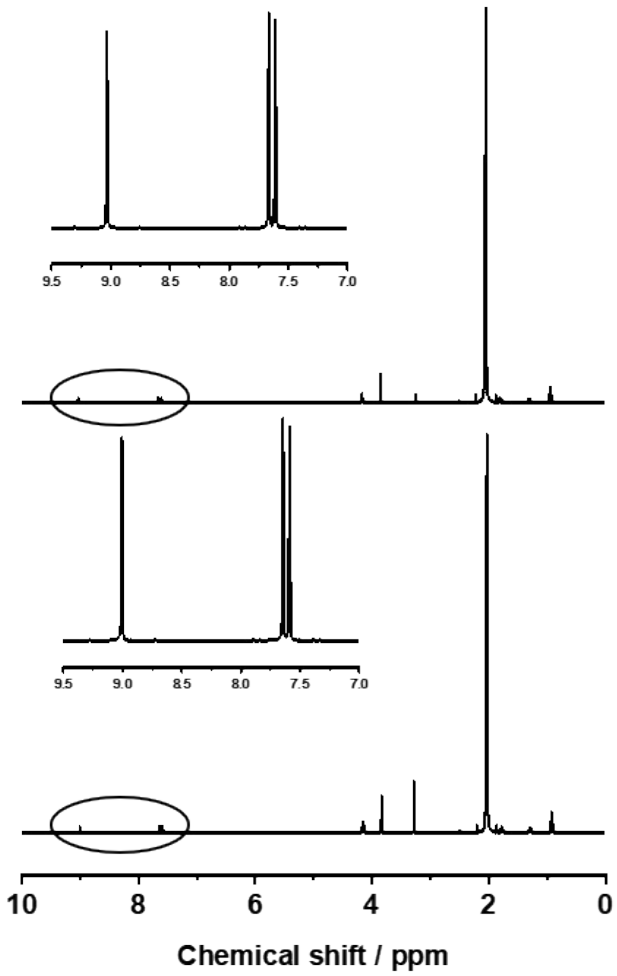

Fig. S11. The ^{1}H-NMR spectra of 0.5 M [Bmim]PF_6/MeCN before (A) and after (B) CO_2 electrolysis on ZnO_{QDs}/P-NC at an applied potential of -2.2 V vs. Ag/Ag^{+} (DMSO-d_6).

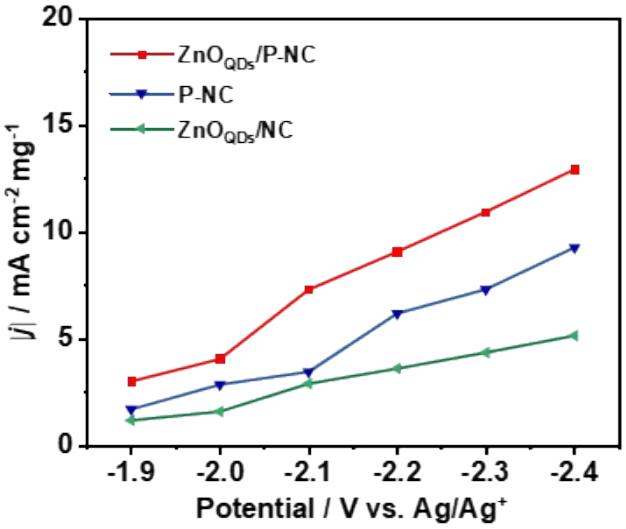

Fig. S12. The partial mass current density for different samples at the applied potentials in 0.5 M [Bmim]PF_6/MeCN electrolyte.

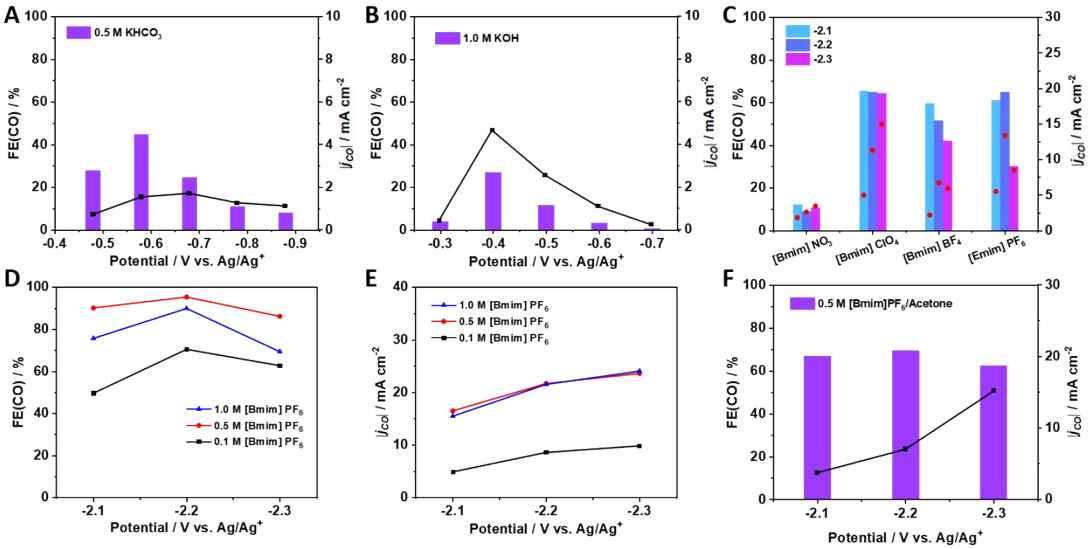

Fig. S13. The current density and the FE(CO) of ZnO_{QDs}/P-NC at the applied potentials in (A) 0.5 M $KHCO_3$ aqueous solution, (B) 1.0 M KOH aqueous solution and (C) different ionic liquid-based electrolytes. (D) The FE(CO) and (E) the current density of ZnO_{QDs}/P-NC at the applied potentials in different concentrations of [Bmim]PF_6/MeCN. (F) The FE(CO) and the current density of ZnO_{QDs}/P-NC at the applied potentials in 0.5 M [Bmim]PF_6/Acetone.

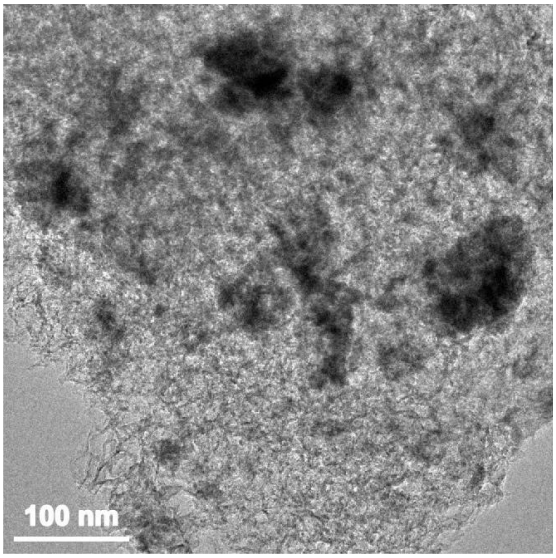

Fig. S14. The HR-TEM image of $ZnO_{25.5\%}$/P-NC.

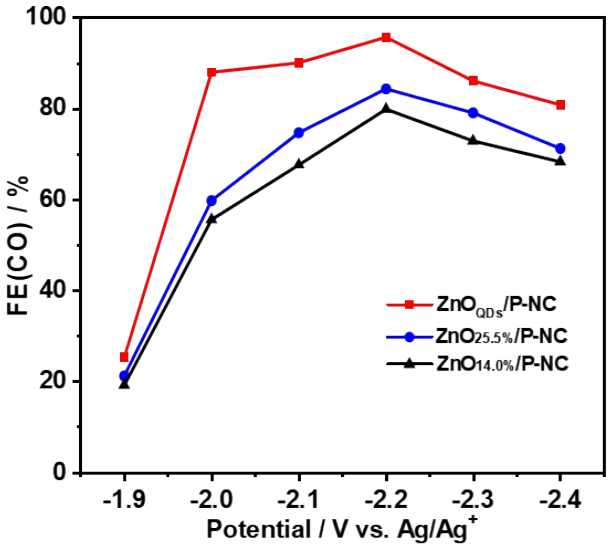

Fig. S15. The FE(CO) of catalysts with different load amounts of ZnO QDs at the applied potentials.

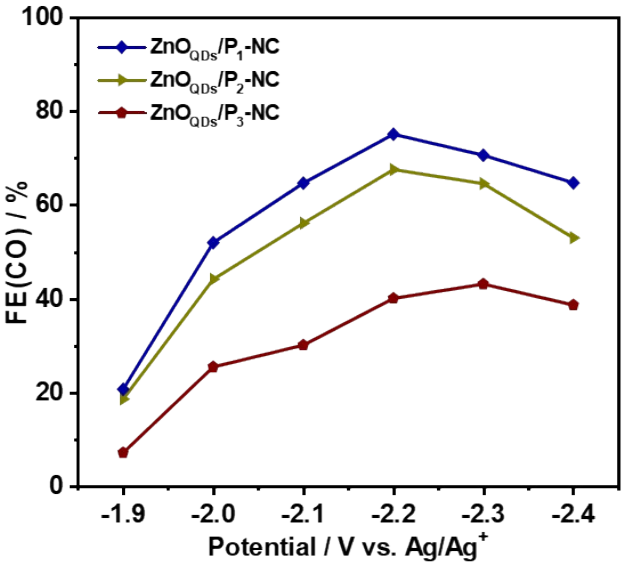

Fig. S16. The FE(CO) of different catalysts of the different pores at the applied potentials.

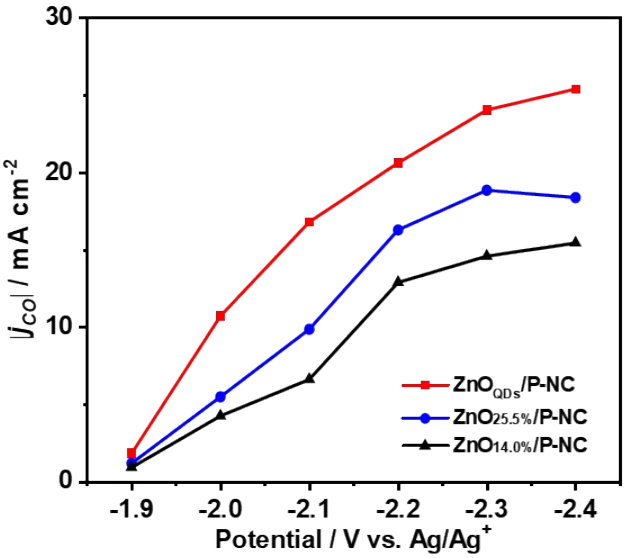

Fig. S17. The current densities of catalysts with different loading amounts of ZnO at the applied potentials.

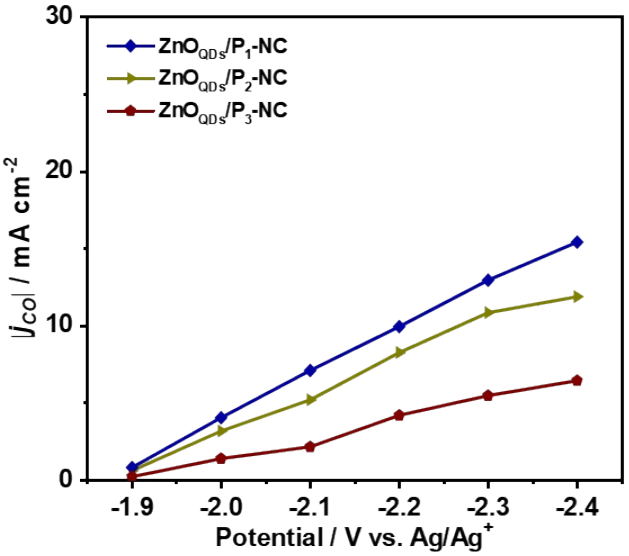

Fig. S18. The current densities of catalysts of the different pores at the applied potentials.

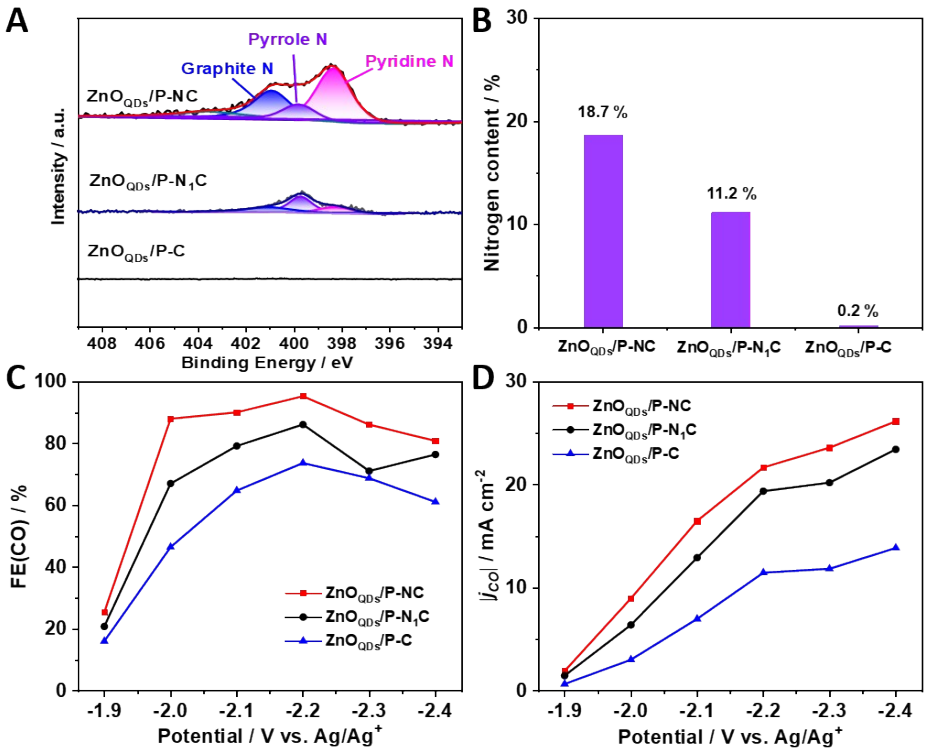

Fig. S19. (A) The XPS spectra of N 1s and (B) the nitrogen content for ZnO_{QDs}/P-NC, ZnO_{QDs}/P-N_1C and ZnO_{QDs}/P-C. (C) The FE(CO) and (D) the current densities of ZnO_{QDs}/P-NC, ZnO_{QDs}/P-N_1C and ZnO_{QDs}/P-C.

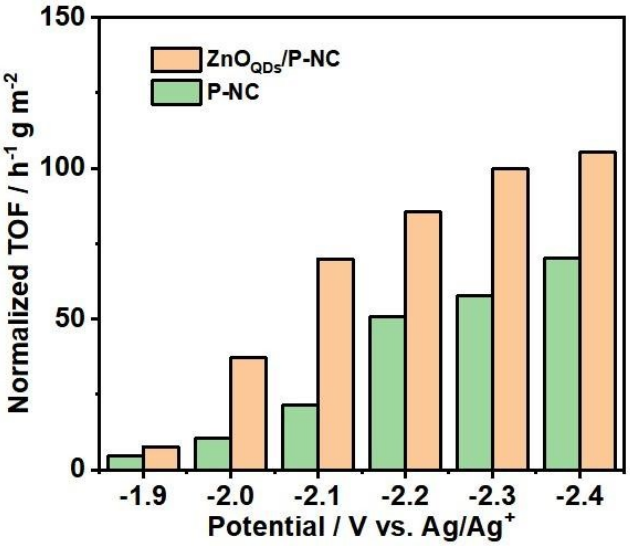

Fig. S20. The BET surface area-normalized turnover frequency (TOF) of CO on N sites for ZnO_{QDs}/P-NC and P-NC.

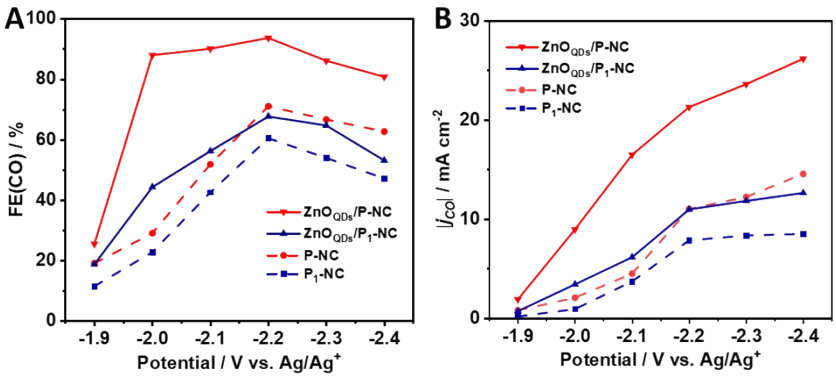

Fig. S21. (A) The FE(CO) and (B) the current densities of ZnO_{QDs}/P-NC, ZnO_{QDs}/P_1-NC, P-NC and P_1-NC.

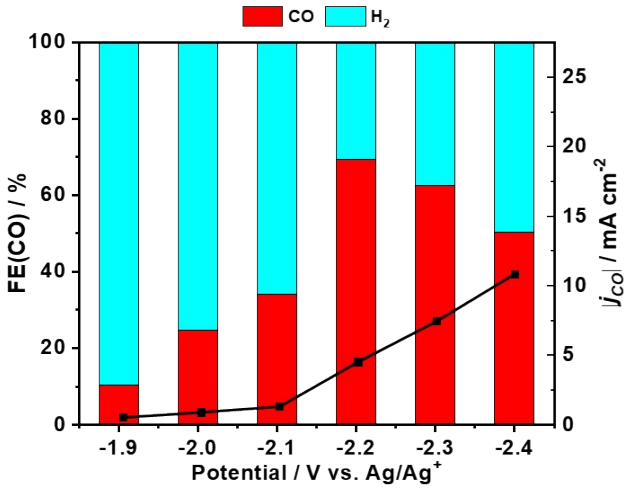

Fig. S22. The FE(CO) and the current densities of ZnO QDs.

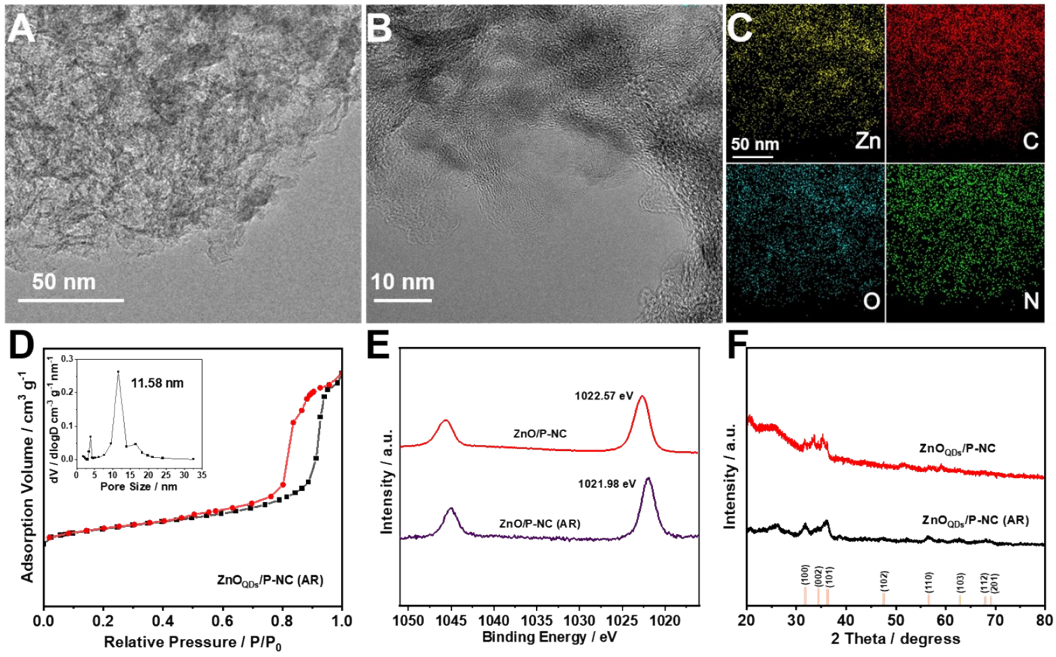

Fig. S23. The TEM image (A), HRTEM image (B), corresponding elemental mappings (C), the N_2-adsorption/desorption isotherms (D, inset: the average pore size distribution), XPS spectrum (E) and XRD pattern (F) of ZnO_{QDs}/P-NC after 2 h electrolysis.

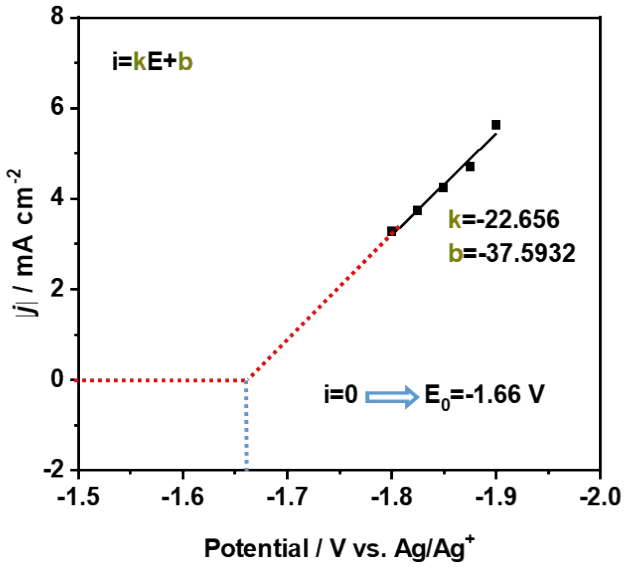

Fig. S24. The extrapolation method of calculating equilibrium potential.

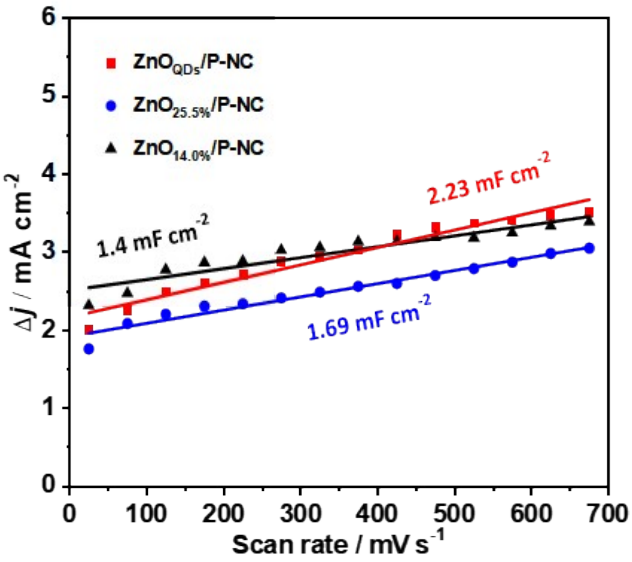

Fig. S25. Charging current density differences plotted against the scan rates for catalysts with different ZnO loads.

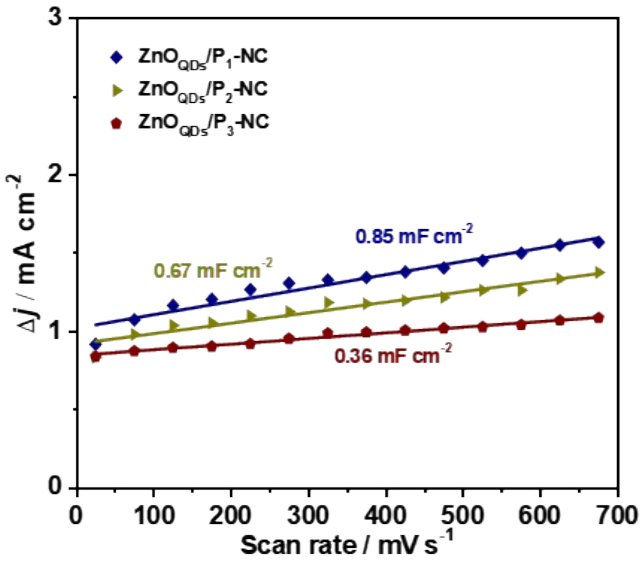

Fig. S26. Charging current density differences plotted against the scan rates for catalysts of the different pores.

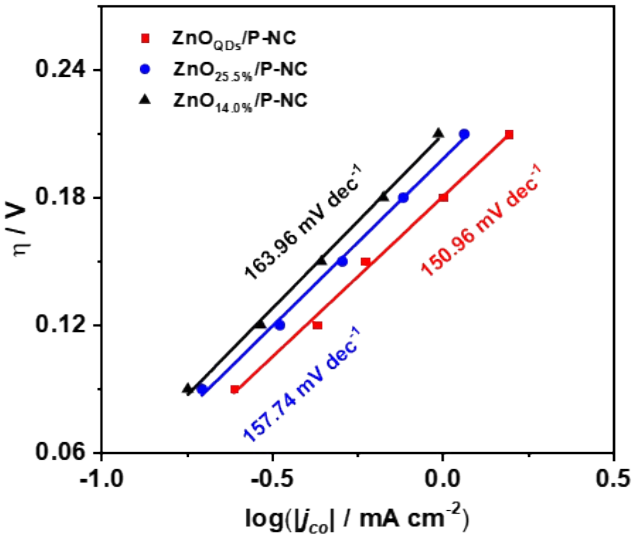

Fig. S27. Tafel plot for CO production over catalysts with different ZnO loads.

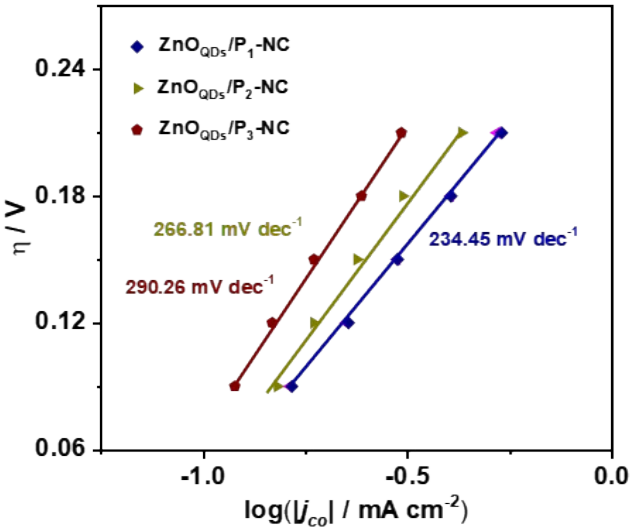

Fig. S28. Tafel plot for CO production over catalysts of the different pores.

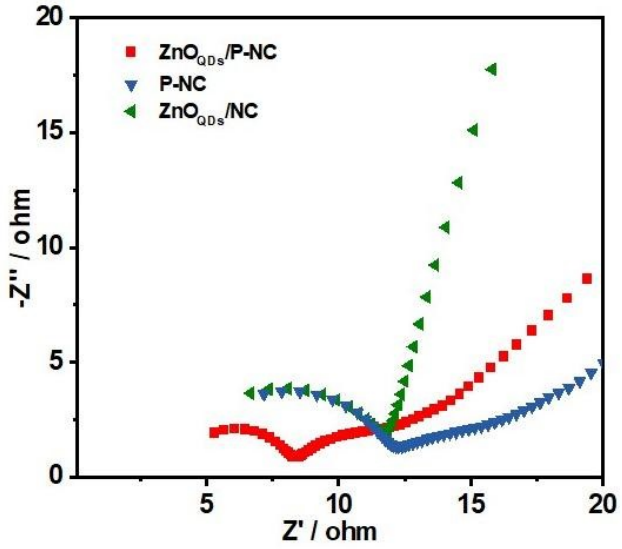

Fig. S29. Nyquist plots for different catalysts in CO_2-saturated 0.5 M [Bmim]PF_6/MeCN electrolyte for different catalysts.

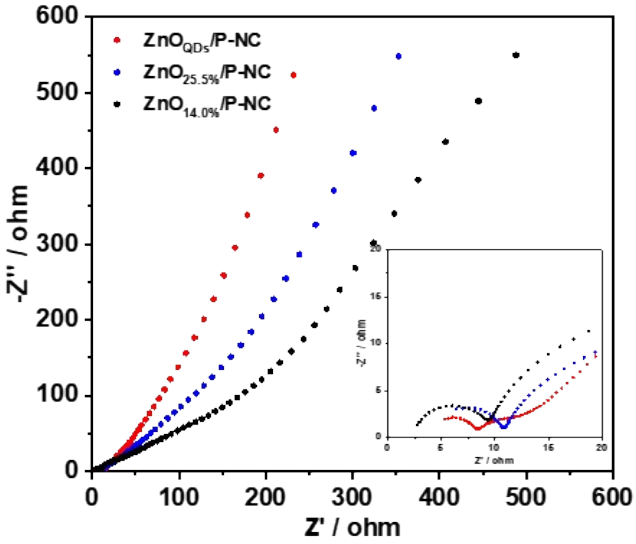

Fig. S30. The Nyquist plots for different catalysts in CO_2-saturated 0.5 M [Bmim]PF_6/MeCN electrolyte for catalysts with different load amounts of ZnO QDs.

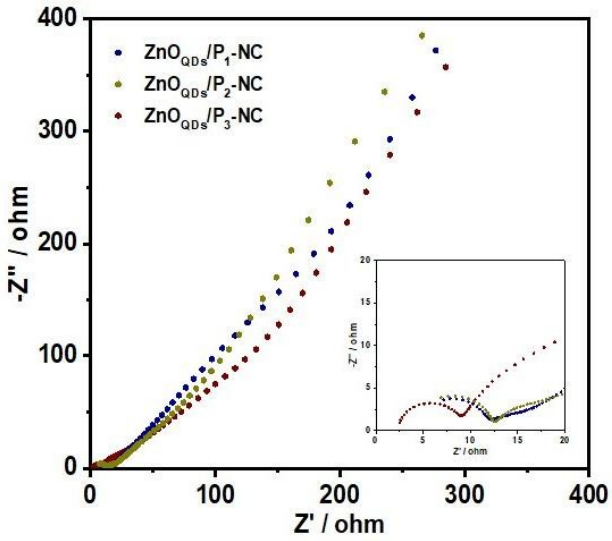

Fig. S31. Nyquist plots for different catalysts in CO_2-saturated 0.5 M [Bmim]PF_6/MeCN electrolyte for catalysts of the different pores.

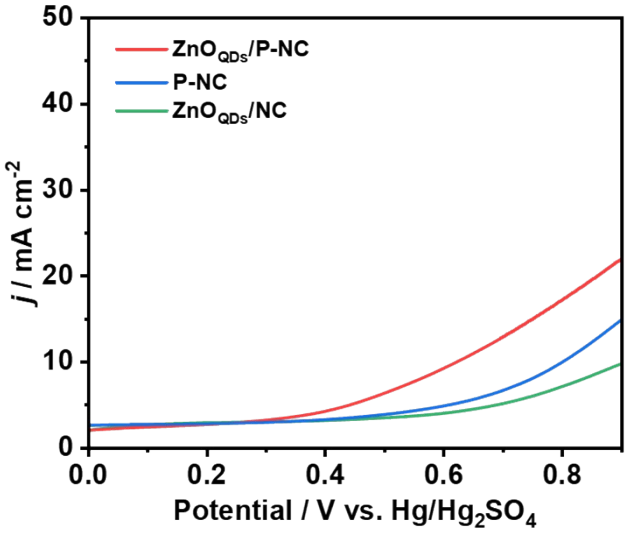

Fig. S32. Single oxidative LSV curves for SO_4^{2-} adsorption over three catalysts in N_2-saturated 0.1 M H_2SO_4.

Supplementary Tables

Table S1. Summary of the amount of colloidal silica and $ZnCl_2$ added, the ICP results, the BET surface area, adsorption average pore size and pore volumes of different catalysts.

Catalysts	Colloidal silica / mL	$ZnCl_2$ / mg	Zn / wt%	BET surface area / $m^2\ g^{-1}$	Adsorption average pore size / nm	Pore volume / $cm^3\ g^{-1}$
P-NC	5	334	0.4	201.7	13.0	1.12
$ZnO_{14.0\%}$/P-NC	5	334	14.0	359.1	11.2	1.26
ZnO_{QDs}/P-NC	5	334	19.3	380.6	11.7	1.08
$ZnO_{25.5\%}$/P-NC	5	334	25.5	374.7	10.8	1.00
P_1-NC	5	0	0	166.3	11.8	1.01
ZnO_{QDs}/P_1-NC	5	0	18.6	206.2	13.5	0.69
ZnO_{QDs}/P_2-NC	2.5	334	17.6	89.0	15.0	0.33
ZnO_{QDs}/P_3-NC	1	334	17.2	20.3	/	0.28
ZnO_{QDs}/NC	0	0	13.8	7.2	/	/

Table S2. CO_2RR performance of ZnO_{QDs}/P-NC in 0.5 M $KHCO_3$ and 1.0 M KOH electrolyte in the flow cell.

Electrolyte	Potential / V *vs.* RHE	$\|j\|$ / mA cm^{-2}	FE(CO) / %
1.0 M KOH	-0.6	59.6	11.52
	-0.7	111.2	15.34
	-0.8	123.2	13.98
0.5 M $KHCO_3$	-0.3	37.8	20.38
	-0.4	53.1	15.05
	-0.5	77.1	11.38

Table S3. CO_2RR performance of ZnO_{QDs}/P-NC with different amounts of Nafion addition in 0.5 M [Bmim]PF_6/MeCN electrolyte.

Amounts of Nafion addition / μL	**$\|j_{CO}\|$ / mA cm^{-2}**	**FE(CO) / %**
0	7.3	53.44
2.5	21.6	95.3
5.0	19.7	94.5

Table S4. The BET surface area and adsorption average pore size of the ZnO_{QDs}/P-NC catalyst obtained after 2 h electrolysis.

BET surface area / m^2 g^{-1}	**Adsorption average pore size / nm**	**Pore volumes / cm^3 g^{-1}**
344.7	11.0	1.05

Table S5. Comparison of the catalytic performance for the ZnO QDs/NC with other catalysts.

Catalysts	Electrolyte	Potential	*j* / mA cm^{-2}	FE(CO) / %	Ref
ZnO_{QDs}/P-NC	0.5 M [Bmim]PF_6/MeCN	-1.34 V *vs.* RHE -2.20 V *vs.* Ag/Ag^+	-21.6	95.3	This work
ZnO sheet array/Zn	0.1 M $KHCO_3$	-1.40 V *vs.* RHE	-11.5	85.0	S1
Vo-rich ZnO	0.1 M $KHCO_3$	-1.10 V *vs.* RHE	-16.0	83.0	S2
Pristine ZnO	0.1 M $KHCO_3$	-1.10 V *vs.* RHE	-7.0	44.0	S2
ZN_X/C	0. 5 M $KHCO_3$	-0.43 V *vs.* RHE	-4.8	95.0	S3
Zn dendrite	0.5 M $KHCO_3$	-0.90 V *vs.* RHE	-4.0	80.0	S4
Zn-N	0.1 M $KHCO_3$	-0.91 V *vs.* RHE	-11.2	85.6	S5
Zn-rich Zn-Cu	0.1 M $KHCO_3$	-0.60 V *vs.* RHE	-3.2	97.0	S6
h-Zn	0.5 M $KHCO_3$	-0.85 V *vs.* RHE	-9.5	80.0	S7
ED Zn	0.5 M $KHCO_3$	-1.10 V *vs.* RHE	-16.0	80.0	S8
LiET-Zn	0.1 M $KHCO_3$	-1.06 V *vs.* RHE	-23.0	43.0	S9
Zn/NC NSs	0.5 M $KHCO_3$	-0.96 V *vs.* RHE	-50.0	95.0	S10
P-Zn	/	-0.95 V *vs.* RHE	-12.7	98.1	S11
Por-Zn	0.1 M $TBAPF_6$ DMF/H_2O	-1.70 V *vs.* SHE	-2.0	95.0	S12

Table S6. Electrocatalytic CO_2RR to CO and H_2 the corresponding equilibrium potentials (E^0, vs. SHE) (25 ℃, 1 atmosphere of gases and 1 M solutes in aqueous solution)

CO_2RR	**E^0 (V *vs.* SHE)**
$CO_2\ (g) + e^- \rightleftharpoons CO_2^{\bullet-}$	-1.900
$CO_2\ (g) + 2H^+ + 2e^- \rightleftharpoons CO\ (g) + H_2O$	-0.530
$CO_2\ (g) + H_2O + 2e^- \rightleftharpoons CO\ (g) + 2OH^-$	-1.347
$2H^+ + 2e^- \rightleftharpoons H_2$	-0.420

Table S7. The C_{dl} of different catalysts.

Catalysts	Slope / mF cm^{-2}	C_{dl} / mF cm^{-2}
ZnO_{QDs}/P-NC	2.23	1.12
P-NC	1.04	0.52
ZnO_{QDs}/NC	0.54	0.27
$ZnO_{14.0\%}$/P-NC	1.40	0.70
$ZnO_{25.5\%}$/P-NC	1.69	0.85
ZnO_{QDs}/P_1-NC	0.85	0.43
ZnO_{QDs}/P_2-NC	0.67	0.34
ZnO_{QDs}/P_3-NC	0.36	0.18

References

1 Q. Xiang, F. Li, J. L. Wang, W. L. Chen, Q. S. Miao, Q. F. Zhang, P. Tao, C. Y. Song, W. Shang, H. Zhu, T. Deng, J. B. Wu, *ACS Appl. Mater.*, 2021, **13**, 10837.

2 Z. G. Geng, X. D. Kong, W. W. Chen, H. Y. Su, Y. Liu, F. Cai, G. X. Wang, J. Zeng, *Angew. Chem. Int. Ed.*, 2018, **57**, 6054.

3 F. Yang, P. Song, X. Z. Liu, B. B. Mei, W. Xing, Z. Jiang, L. Gu, W. L. Xu, *Angew. Chem. Int. Ed.*, 2018, **57**, 12303.

4 J. Rosen, G. S. Hutchings, Q. Lu, R. V. Forest, A. Moore, F. Jiao, *ACS Catal.*, 2015, **5**, 4586.

5 W. N. Deng, S. X. Min, F. Wang, Z. G. Zhang, C. Kong, *Dalton Trans.*, 2020, **49**, 5434.

6 L. Wang, H. Peng, S. Lamaison, Z. Qi, D. M. Koshy, M. B. Stevens, D. Wakerley, J. A. Zamora Zeledón, L. A. King, L. Zhou, Y. Lai, M. Fontecave, J. Gregoire, F. Abild-Pedersen, T. F. Jaramillo, C. Hahn, *Chem Catalysis*, 2021, **1**, 663.

7 D. H. Won, H. Shin, J. Koh, J. Chung, H. S. Lee, H. Kim, S. I. Woo, *Angew. Chem. Int. Ed.*, 2016, **55**, 9297.

8 Y. Lu, B. Han, C. C. Tian, J. Wu, D. S. Geng, D. W. Wang, *Electrochem Commun.*, 2018, **97**, 87.

9 K. Jiang, H. Wang, W. B. Cai, H. T. Wang, *ACS Nano*, 2017, **11**, 6451.

10 J. Y. Chen, Z. J. Li, X. Y. Wang, X. H. Sang, S. X. Zheng, S. J. Liu, B. Yang, Q. H. Zhang, L. C. Lei, L. M. Dai, Y. Hou, *Angew. Chem. Int. Ed.*, 2022, **61**, e202111683.

11 Y. Feng, C. Q. Cheng, C. Q. Zou, X. L. Zheng, J. Mao, H. Liu, Z. Li, C. K. Dong, X. W. Du, *Angew. Chem. Int. Ed.*, 2020, **59**, 19297.

12 Y. S. Wu, J. B. Jiang, Z. Weng, M. Y. Wang, D. Broere, Y. R. Zhong, G. Brudvig, Z. X. Feng, H. L. Wang, *ACS Cent. Sci.*, 2018, **256**, 847.